Observation of the strain-driven charge-ordered state in La$_{0.7}$Ca$_{0.3}$MnO$_{3-\delta}$ thin film with oxygen deficiency

V.G. Prokhorov, V.A. Komashko, and G.G. Kaminsky

Institute of Metal Physics, National Academy of Sciences of Ukraine,
36 Vernadsky Ave., Kiev, 03142, Ukraine
E-mail: pvg@imp.kiev.ua

V.L. Svetchnikov and H.W. Zandbergen

NCHREM, Rotterdamseweg 137, 2628AL, Delft, The Netherlands

Y.P. Lee and J.S. Park

Department of Physics, Hanyang University, Seoul, 133-791 Korea

K.W. Kim

Department of Physics, Sunmoon University, Choongnam, 336-840 Korea

The magnetic and transport properties of La$_{0.7}$Ca$_{0.3}$MnO$_{3-\delta}$ films with an oxygen deficiency ($\delta \simeq 0.1$) and a La$_{0.9}$Ca$_{0.1}$MnO$_3$ film with the stoichiometric oxygen content are investigated in a wide temperature range. It is shown that the charge-ordered insulating (COI) state is observed for a La$_{0.7}$Ca$_{0.3}$MnO$_{2.9}$ film with thickness $d \leq 30$ nm, which manifests mainly a cubic crystal structure with an anomalously small lattice parameter for this composition. An increase in the film thickness ($d \simeq 60$ nm) leads to a structural transition from the lattice-strained cubic to the relaxed rhombohedral phase, is accompanied by a shift of the Curie point (T_C) to lower temperature and a frustration of the COI state. The magnetic and transport properties of the La$_{0.7}$Ca$_{0.3}$MnO$_{2.9}$ film with $d \simeq 60$ nm are similar to those exhibited by the optimally oxygen-doped La$_{0.9}$Ca$_{0.1}$MnO$_3$ film. It is concluded that the formation of the COI state in the La$_{0.7}$Ca$_{0.3}$MnO$_{3-\delta}$ compound is governed by a compression of the crystal lattice rather than accumulation of oxygen vacancies, the low doping of the substituted divalent ions, or electronic phase separation.

PACS: **71.30.+h**, 75.30.Vn, **75.70.−i**

1. Introduction

The hole-doped perovskite manganites are of great current interest not only because of their interesting fundamental science, connected with the discovery of colossal magnetoresistance (CMR), but also in connection with their potential applications to new devices such as magnetic read heads, field sensors, and memories. Recently evidence was presented for the co-existence at low temperatures of ferromagnetic metallic (FMM) and charge-ordered insulating (COI) phases in La$_{0.67}$Ca$_{0.33}$MnO$_3$ films, governed by the lattice strains accumulated during the deposition [1,2]. That is contradicted by the common knowledge that the phenomenon of charge ordering (CO) is observed only in compounds with a small average A-site cation radius, $\langle r_A \rangle \leq 0.118$ nm. However, in view of the very similar energies of the COI and FMM states in these compounds [3], one might expect the appearance of COI regions in a compound with a larger $\langle r_A \rangle$ induced by a structural distortion away from the ideal cubic perovskite lattice [2]. It is believed that the stoichiometric compound LaMnO$_3$ (Mn^{3+}; $t_{2g}^3 e_g^1$) is antiferromagnetic due to the superexchange coupling between Mn^{3+} ions. A partial substitution of the trivalent La^{3+} by divalent Ca^{2+} ions is balanced by a conversion of the Mn valence states between Mn^{3+} and

Mn^{4+}, which leads, first, to an increase of the Curie point (T_C) and, second, to the formation of the FMM state in the temperature range $T \le T_C$ at a certain concentration of Ca. However, a change in the Mn^{3+}: Mn^{4+} ratio can be produced by the creation of vacancies at the oxygen sites, as well. The oxygen deficiency leads to a degradation in the Curie point and in the temperature of the metal—insulator (MI) transition, providing the formation of the COI state in the manganites [4–11]. The other point of view is based on the idea of the electronic phase separation between phases with different hole densities in the low-doped manganites, which can also induce the coexisting nano-scale metallic and insulating clusters [12]. Therefore, it is not clear what is the main reason for the appearance of the COI state in these materials — lattice strains, oxygen vacancies, or low doping of the substituted divalent ions.

In this paper we report experimental results for $La_{0.7}Ca_{0.3}MnO_{3-\delta}$ films with an oxygen deficiency ($\delta \simeq 0.1$) and $La_{0.9}Ca_{0.1}MnO_3$ film with the stoichiometric oxygen content. It was found that the COI state is observed only for $La_{0.7}Ca_{0.3}MnO_{2.9}$ films with thickness $d \le 30$ nm, which manifest mainly a cubic crystal structure with an anomalously small lattice parameter for this composition. The increase in the film thickness ($d \simeq 60$ nm) leads to a structural transition from the lattice-strained cubic to the relaxed rhombohedral phase, which is accompanied by a shift of the Curie point to lower temperature and a frustration of the COI state. The magnetic and transport properties of the $La_{0.7}Ca_{0.3}MnO_{2.9}$ film with $d \simeq 60$ nm become similar to those exhibited by the optimally oxygen-doped $La_{0.9}Ca_{0.1}MnO_3$ film. Therefore the formation of the COI state in the $La_{0.7}Ca_{0.3}MnO_{3-\delta}$ compound is governed by a compression of the crystal lattice rather than accumulation of oxygen vacancies, the low doping of the substituted divalent ions, or electronic phase separation.

2. Experimental techniques

All the films were prepared by rf magnetron sputtering using a so-called «soft» (or powder) target [13]. The total pressure in the chamber was $5 \cdot 10^{-2}$ Torr with a gas mixture of Ar and O_2 (3 : 1). The substrate was a $LaAlO_3$ (001) single crystal with a lattice parameter $a \simeq 0.379$ nm for the pseudocubic symmetry. The substrate temperature during deposition was 750°C. Under these conditions we deposited two $La_{0.7}Ca_{0.3}MnO_{3-\delta}$ films with different thickness: $d \le 30$ nm (LCM1) and $d \simeq 60$ nm (LCM2). The stoichiometric $La_{0.9}Ca_{0.1}MnO_3$ (LCM3) film with $d \simeq 60$ nm was made by additional postannealing at

800°C in 1-atm O_2 for 1.5 h. The θ–2θ x-ray diffraction (XRD) patterns were obtained using a Rigaku diffractometer with CuK_{α} radiation. The lattice parameters evaluated directly from the XRD data were plotted against $\cos^2 \theta / \sin \theta$. With an extrapolated straight line to $\cos^2 \theta / \sin \theta = 0$, a more precise determination of the lattice parameter was obtained. The high-resolution electron microscopy (HREM) studies were carried out using a Philips CM300UT-FEG microscope with a field emission gun operated at 300 kV. The point resolution of the microscope is of the order of 0.12 nm. Cross-section specimens were prepared by the standard techniques using mechanical polishing followed by ion-beam milling under grazing incidence. The resistance measurements were carried out by the four-point-probe method in a temperature range of 4.2–300 K and a magnetic field up to 5 T. The magnetization in a field up to 100 Oe were taken with a Quantum Design SQUID magnetometer in a temperature range of 4.2–300 K.

3. Microstructure of the films

Figure 1,*a* presents the (002) Bragg peaks for the LCM1 (*1*), LCM2 (*2*), and LCM3 (*3*) films. It is seen that the LCM2 and LCM3 films display only one peak, which corresponds to an out-of-plane lattice parameter for the cubic symmetry *c* of 0.3947 nm and
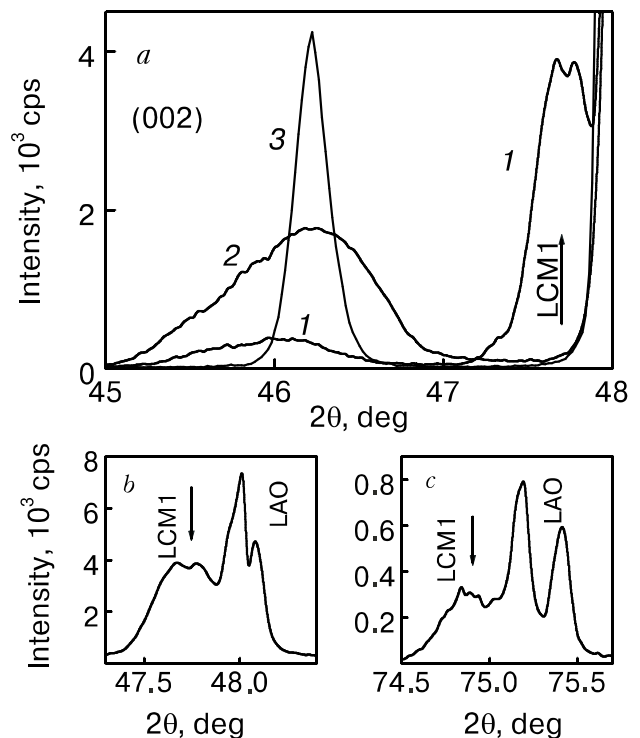

Fig. 1. (*a*) The (002) XRD peaks for LCM1 (*1*), LCM2 (*2*), and LCM3 (*3*) films. (*b*) and (*c*) are the (002) and (003) peaks, respectively, of the LCM1 film.

0.3923 nm, respectively. The thinner LCM1 film manifests two Bragg peaks. The first of them (lower-intensity) indicates $c \simeq 0.394$ nm, which is almost coincident with the lattice parameters of LCM2 and LCM3 films. The second is located very close to the substrate peak and corresponds to $c \simeq 0.3795$ nm. Figures 1,b and 1,c show the high-angle peaks of the (002) and (003) reflections, respectively, in detail for the LCM1 film. It is noteworthy that a similar asymmetry of the substrate Bragg peak was observed recently by Li et al. [9], but without discussion. Therefore, the XRD data testify that the LCM1 film contains two crystalline phases with different lattice parameters, in contrast to the LCM2 and LCM3 films. The first phase with a larger c belongs to a relaxed state of the crystal lattice for $La_{0.7}Ca_{0.3}MnO_{3-\delta}$ with oxygen deficiency (A-phase). This interpretation is supported by the large value for the out-of-plane lattice parameter, which differs greatly from the stoichiometric one for this composition ($c \simeq 0.3849$ nm) [7]. Using the empirical ratio between the oxygen deficiency δ and the out-of-plane lattice parameter [11], we estimated the value of δ for the A-phase to be $\delta \simeq 0.1$. The second crystalline phase (B-phase) with an unusually small lattice parameter, in view of the large peak intensity, can be considered as the primary peak of the LCM1 film. The small value for the lattice parameter is provided by epitaxial growth of the film and the accumulation of a biaxial compressive lattice strain. An increase in the film thickness leads to a recrystallization during deposition or cooling of the film and results in the disappearance of the B-phase, which is inferred from the absence of the second Bragg peak (curve 2 in Fig. 1,a). The estimated value for oxygen deficiency of the LCM2 film is $\delta \simeq 0.11$ and is almost identical with that for the A-phase of LCM1. Note that the results obtained coincide excellently with the published data for similarly oxygen-deficit films [14].

The cross-section low-magnification HREM images of the studied films are shown in Fig. 2. They were obtained with the incident beam parallel to a cube direction of the substrate and parallel to the film/substrate interface. All films are epitaxial and exhibit sharp, flat, and well-defined interfaces. However, it is seen that the structure changes slightly for different films. The LCM1 film with smallest thickness (Fig. 2,a) exhibits a perfect single-crystal structure. It shows uniform contrast; neither dislocations nor domains were observed. The LCM2 and LCM3 films (Figs. 2,b and 2,c, respectively) exhibit a set of regions with a slightly different brightness, which can be treated as a presence of the crystalline domains separated by the lattice strain (shown by the white arrows) [15]. Moreover, in the LCM2 film the dark con-
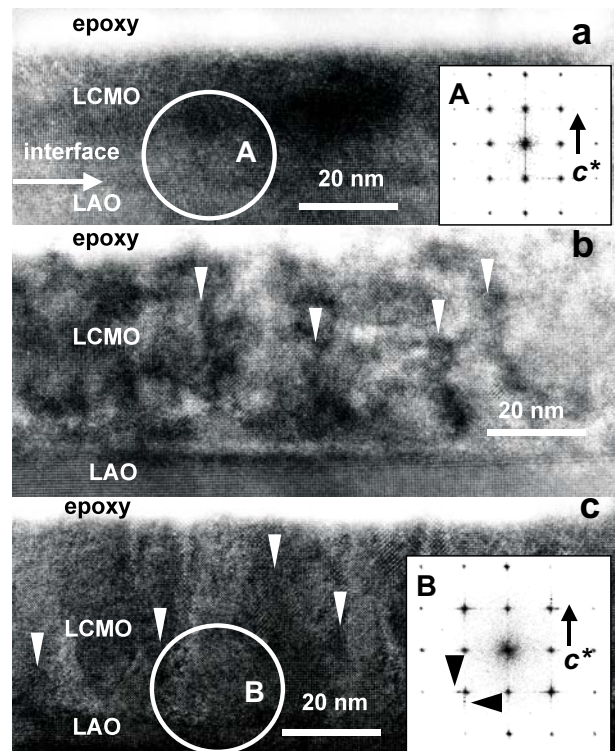

Fig. 2. Low-magnification HREM images of a cross section for LCM1 (*a*), LCM2 (*b*), and LCM3 (*c*) films. The insets are the FFT of the areas A and B containing the interface for the LCM1 and LCM3 films, respectively.

trast demonstrates the more or less disordered zones, suggesting the formation of the chaotic domain structure, while in the LCM3 film the columnar microstructure occurs with columns parallel to the interface normal. The inset in Fig. 2,a shows the fast Fourier transform (FFT) of the HREM image (area A) for LCM1 film selected across the interface. It is seen that the FFT of an area containing the interface produces a rectangular pattern of the circled and unsplitted spots. Therefore, the out-of-plane (*c*) and in-plane (*a*) lattice parameters are the same for both the substrate and the film. Their value is coincident with the XRD data for the B-phase of the LCM1 film with the smallest lattice parameter $c \simeq 0.3795$ nm. The more detailed analysis of the HREM images of the LCM1 film shows that the inclusions of the A-phase with the lattice parameter $c \simeq 0.39$ nm are present near the top of the film.

The inset in Fig. 2,c shows the FFT of the HREM image (area B) for the LCM3 film selected across the interface, as well. In this case the FFT pattern for the similar area containing the interface displays the spots elongated and slightly split in the *c* (along to the interface normal) and *a* (along to the interface) directions (shown by black arrows). One can conclude that
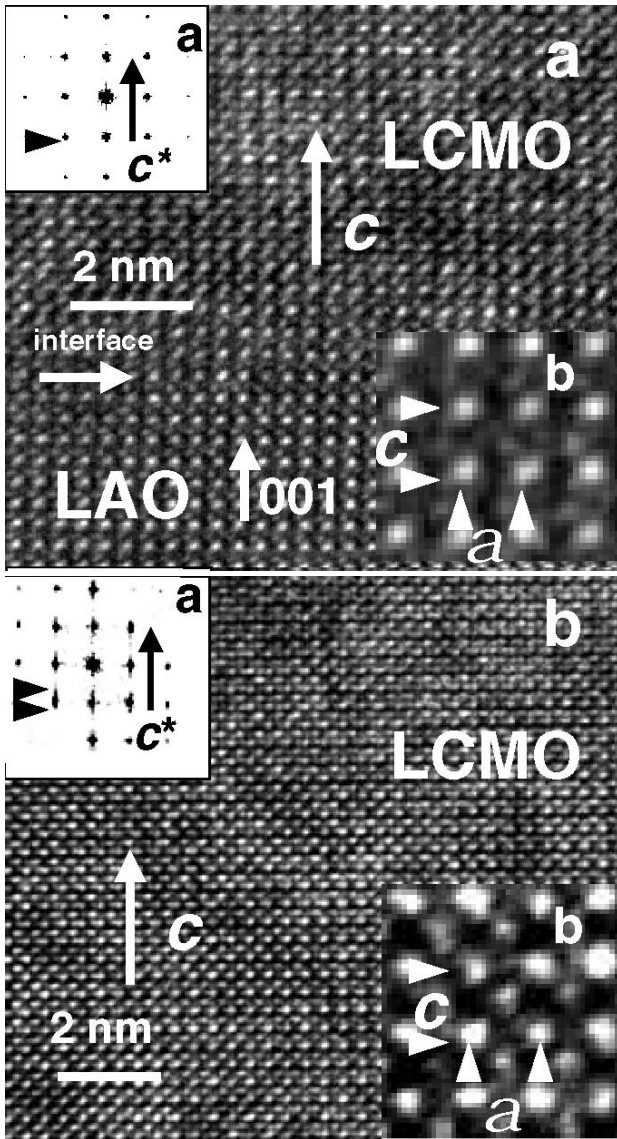
Fig. 3. HREM images of a cross section for LCM2 film near the interface (*a*) and 30 nm about it (*b*). The insets *a* are the FFT of the corresponding areas of the film. The insets *b* are high-magnification HREM images for the substrate (top) and the film (bottom).

the interface is incoherent in the LCM3 film, providing the difference in the lattice parameters of the substrate and the film. A similar FFT pattern was obtained for the area of the LCM2 film containing the interface, which is reproduced in inset *a* of Fig. 3,*a*. In contrast to that the FFT pattern for the area of the film located 30 nm above the interface exhibits spots elongated only in the *c* direction (see inset *b* in Fig. 3,*b*). We attribute these features to the slight tetragonal deformation of the crystal lattice in the LCM2 film.

The insets *b* in Figs. 3,*a* and 3,*b* show the high-magnification HREM images of LCM2 film for the substrate and the film, respectively. The brightest

dots represent La(Ca) atoms in the film as well as in the substrate. The less bright dots at the centers of the squares of brightest dots represent AlO chains in the substrate and MnO chains in the film. The measurement of a large number of interdot spacings allow us to obtain the average values of the lattice parameters from the HREM images. According to analysis one can conclude that the LaAlO$_3$ substrate has a pseudocubic crystal lattice with $c \simeq a \simeq 0.379$ nm and angle of the cell $\alpha_C \simeq 90°$, and the greater part of the LCM1 film has also a pseudocubic crystal lattice with $c \simeq a \simeq 0.379$ nm and $\alpha_C \simeq 90°$ (except for local areas near the top of the film, which have a rhombohedral crystal structure with $c \simeq a \simeq 0.39$ nm and $\alpha_C \simeq 90.4°$). The LCM2 and LCM3 films have a similar rhombohedral crystal structure with $c \simeq a \simeq 0.395$ nm and $\alpha_C \simeq 90.6°$, and $c \simeq a \simeq 0.391$ nm and $\alpha_C \simeq 90.6°$, respectively. It is seen that results obtained agree very perfectly with the XRD data for the investigated films.

Therefore, both the cubic (*B*-phase) and the rhombohedral (*A*-phase) crystalline phases coexist in LCM1 while only the rhombohedral phase exists in LCM2 and LCM3. An estimation of the average crystallite size (*D*) using the Scherrer formula for the Bragg peak broadening shows that the LCM1 film consists of the large-size grains ($D \approx 50$ nm) belonging to the *B*-phase and small-size clusters ($D \approx 7-10$ nm) in the *A*-phase. For LCM2 and LCM3 the average size of the crystallites turns out to be about $D \approx 10-12$ nm and 60 nm, respectively. The sizes obtained are supported by the peculiarities of the contrast in the HREM images (Fig. 2) and agree with the published results for thin films of similar compositions [16,17]. The large difference in crystallite size between the *A*- and *B*-phase indicates that the cubic *B*-phase is formed directly during deposition, while the rhombohedral *A*-phase is made during the recrystallization afterwards.

4. Experimental results

Figure 4 displays the temperature dependence of the resistance $R(T)$ for the LCM1 film without (*1*) and with (*2*) an applied magnetic field of 5 T. The magnetic field was directed at right angles to both the film surface and the transport current. The experimental curves attest to the existence of two phases with different temperatures for the MI transition in the applied magnetic field. The first phase undergoes a transition from the insulating to the metallike state at $T_{P1} \approx 200$ K, which agree perfectly with recently published results obtained for a similar thin film with oxygen stoichiometry [2]. The second phase manifests
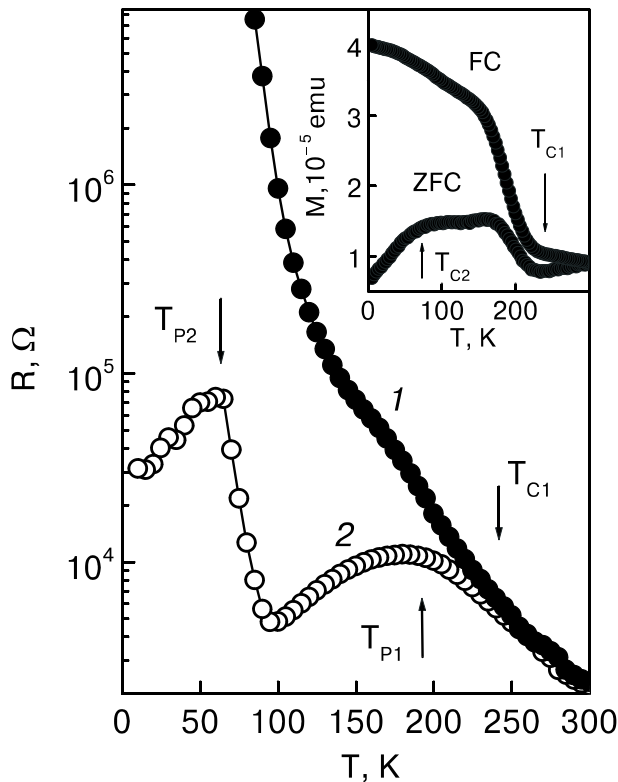
Fig. 4. Temperature dependence of the resistance for LCM1 film without (*1*) and with (*2*) an applied magnetic field of 5 T. The lines are a guide to the eye. The inset displays the temperature dependence of the field-cooled and zero-field-cooled magnetization for this film.

Fig. 5. Temperature dependence of the resistance for the LCM2 film without (*1*) and with (*2*) an applied magnetic field of 5 T. The lines are a guide to the eye. The inset *a* displays the temperature dependence of the FC and the ZFC magnetization. The inset *b* shows the temperature dependence of the magnetoresistance in an applied magnetic field of 5 T.

the MI transition at $T_{P2} \simeq 80$ K. In zero applied magnetic field both phases display an exponential growth of the resistance with decreasing temperature. Unfortunately, our setting was limited to 10^7 Ω and we could not measure $R(T)$ down to the lowest temperature. The inset in Fig. 4 reveals that both field-cooled (FC) and zero-field-cooled (ZFC) magnetization curves represent a superposition of the two magnetic transitions belonging to the different phases. The onset of the magnetic transition is observed at $T_{C1} \simeq 230$ K for the first phase and at $T_{C2} \approx 100$ K for the second phase.

Figure 5 show that the LCM2 film does not undergo the MI transition in the investigated temperature range, even though negative magnetoresistance (MR) appears at $T \leq 150$ K, as in inset *b*. The MR value is defined by MR $= 100\% \, [R(0) - R(H)] / R(H)$ where $R(0)$ and $R(H)$ are resistances with and without magnetic field, respectively. Inset *a* of Fig. 5 shows that the magnetic transition in this film begins at $T_C \simeq 120$ K that is coincident with the onset for the second magnetic transition in LCM1. Because the lattice parameter *c* of the LCM2 film is similar to that for the *A*-phase of LCM1 film, it is reasonable to assert
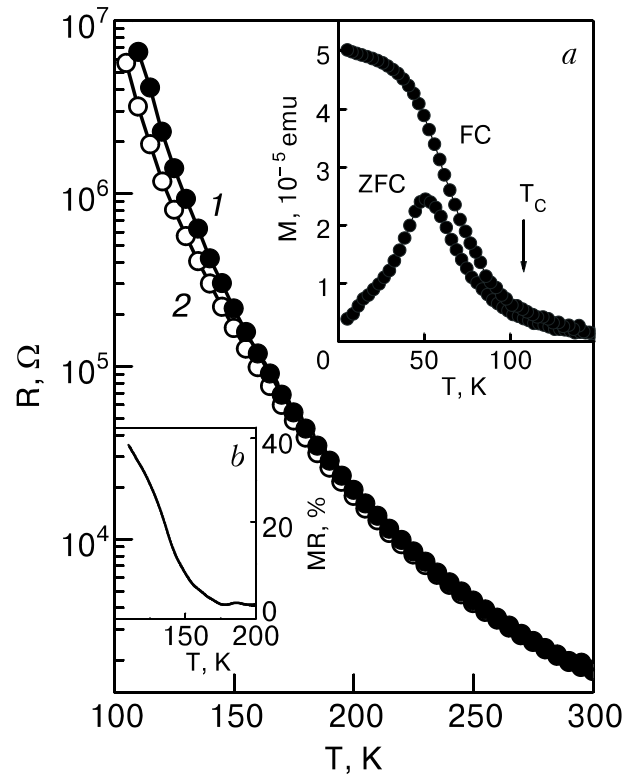
that the *A*-phase shows the magnetic and electronic transitions at a low temperature (T_{C2} and T_{P2} in Fig. 4).

Figure 6 exhibits the magnetic and transport properties for the LCM3 film. Inset *b* shows that the MR(*T*) demonstrates a peaklike behavior with $T_P \simeq 150$ K that is coincident with the temperature of the magnetic transition, T_C. The unusual FC $M(T)$, revealing a drop of the magnetization at T 120 K (inset *a* in Fig. 6) can be explained by the existence of a second ferromagnetic→canted antiferromagnetic transition in this film, with $T_N \simeq 118$ K [18]. We suggest that it is the main reason for the peaklike behavior of MR(*T*) for the LCM3 film.

5. Discussion

The temperature behavior of the resistance for the *B*-phase of the LCM1 film in an applied magnetic field (curve *2* in Fig. 2) is very similar to that for a thin $La_{0.67}Ca_{0.33}MnO_3$ film in the COI state as reported by Biswas et al. [2]. Consequently, the transition of the *B*-phase at $T \leq 210$ K from the insulating to the metallic state under applied magnetic field (curve *2* in
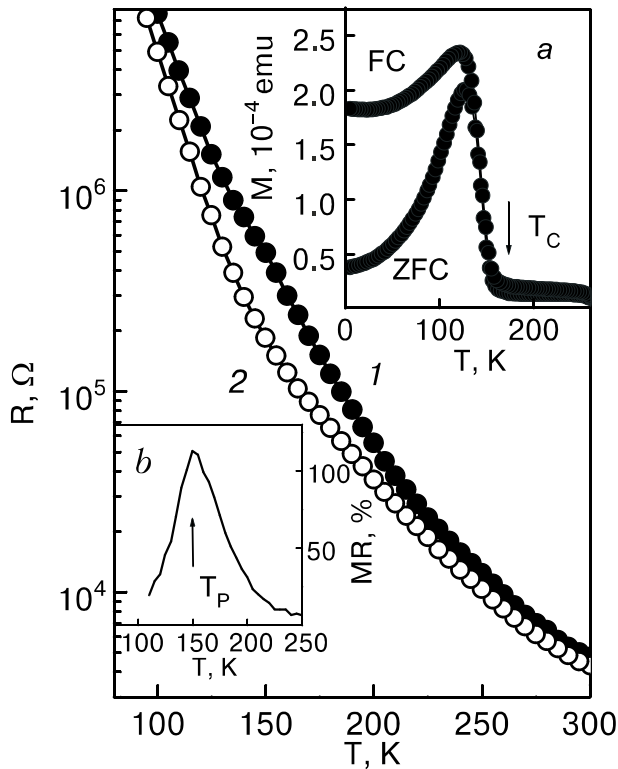
Fig. 6. Temperature dependence of the resistance for LCM3 film without (*1*) and with (*2*) an applied magnetic field of 5 T. The lines are a guide to the eye. The inset *a* shows the temperature dependence of the FC and ZFC magnetization. The inset *b* displays the temperature dependence of the magnetoresistance in an applied magnetic field of 5 T.

Fig. 4) can be treated as melting of the COI state and nucleation of the FMM phase with decreasing temperature. The observed increase in resistance at $T \leq 100$ K (curve *2* in Fig. 4) testifies that the inclusions of the *A*-phase remain in the paramagnetic insulating (or semiconducting) state up to $T_{P2} \simeq 80$ K. The authors [1,2] presented an explanation for appearance of the COI state in thin manganite films, based on the idea of a nonuniform distribution of the lattice strain that resulted from a transition from a two- to a three-dimensional growth mode. It was suggested that the two-phase state is formed by separation of the film into high-strain and strain-free regions which possess different transport and magnetic behaviors at low temperatures. However, in our case the oxygen-deficit $La_{0.7}Ca_{0.3}MnO_{2.9}$ thin film is separated into two different *crystalline* phases, and only the cubic phase with an anomalously small lattice parameter gives evidence for the COI state. It is reasonable to claim that the forced reduction of the lattice parameter, induced by the epitaxial growth mode, is equivalent to a decrease in the average *A*-site cation radius, $\langle r_A \rangle$, which makes this compound similar to

$Pr_{0.7}Ca_{0.3}MnO_3$. It was shown recently that an increase of the out-of-plane lattice parameter of a $Pr_{0.65}Ca_{0.35}MnO_3$ film leads to frustration of the COI state [8−20]. Here we observe the opposite phenomenon, which is connected with the appearance of the COI state in the $La_{0.7}Ca_{0.3}MnO_{2.9}$ thin film with an artificially reduced lattice parameter.

The $La_{1-x}^{3+}Ca_x^{2+}Mn_{1-x+2\delta}^{3+}Mn_{x-2\delta}^{4+}O_{3-\delta}^{2-}V_\delta^0$ is ionic structure of manganites according to Jonker and van Santen [21], where V_δ^0 stands for the ratio of oxygen vacancies. Consequently, the real Mn^{3+} : Mn^{4+} ratio in the LCM1 and LCM2 films is about 0.9:0.1 instead of 0.7:0.3. A similar Mn^{3+} : Mn^{4+} ratio is applies to the LCM3 film with the optimum oxygen doping. Therefore, the concentration of Mn^{4+} ions in the *A*-phase of LCM1 is about equal to that in the LCM2 and LCM3 films. However, the manganese valency is provided by the oxygen deficiency in the case of LCM1 (*A*-phase) and LCM2 but by the concentration of the substituted divalent ions in the case of LCM3. In the both cases the decrease in the concentration of Mn^{4+} ions reduces the Curie temperature and leads to suppression of the MI transition for this compound [11,22]. On the other hand, our results show that the artificial compression of the unit cell volume leads to a significant increase in the Curie temperature (down to value which is typical for the stoichiometric composition), in spite of the remaining deficiency of Mn^{4+} ions.

Figure 7 shows the ln (R/T) versus T^{-1} plots for the LCM1 (*1*), LCM2 (*2*), and LCM3 (*3*) films. In the high-temperature range the plots can be described on the basis of thermally-activated conductivity (TAC) model, which predicts an expression $R(T) = R_0T \exp(T_A/T)$, where T_A is the activation energy in units of temperature. The inset displays that the best agreement between the experiment and the theory (solid lines) is seen with the following fitting parameters: $R_0 \simeq 5.78 \cdot 10^{-2}$ Ω and $T_A \simeq 1470$ K for LCM1, $R_0 \simeq 2.38 \cdot 10^{-2}$ Ω and $T_A \simeq 1680$ K for LCM2, and $R_0 \simeq 4.5 \cdot 10^{-2}$ Ω and $T_A \simeq 1700$ K for LCM3. The values for the activation energy turn out to be almost identical for the LCM2 and LCM3 films. Taking into account that both films have a rhombohedral crystal structure and similar hole densities (similar Mn^{3+} : Mn^{4+} ratios), the obtained result is absolutely expected. The LCM1 film, most of which is in a cubic *B*-phase, shows a smaller value of T_A. It can be explained by the significant difference in the Mn−O−Mn angle between these two kinds of films, which plays a key role for the mechanism of transport in manganites. The arrows in Fig. 7 indicate the onset of magnetic transitions in the LCM3 film and the *B*-phase of LCM1 film. Near these temperatures the $R(T)$ behavior is changed for both films. The absence
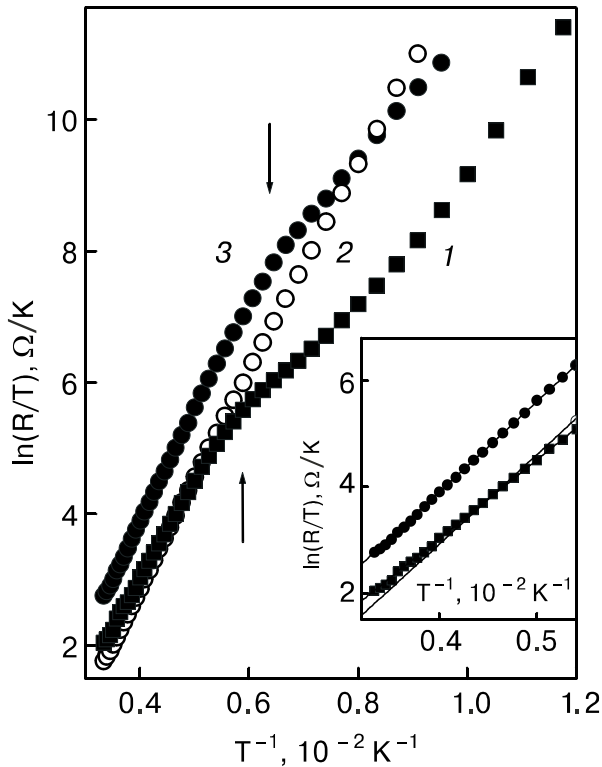
Fig. 7. ln (R/T) versus T^{-1} for LCM1 (*1*), LCM2 (*2*), and LCM3 (*3*) films without an applied magnetic field. The inset displays the high-temperature range. The solid lines are fitting curves based on the TAC model.

of such a peculiarity in $R(T)$ for the LCM2 film is explained by the limited capability for measurements in the low-temperature region or a very small value of the magnetization compared with the LCM3 film (see insets *a* in Figs. 5 and 6).

6. Conclusion

The magnetic and transport properties of $La_{0.7}Ca_{0.3}MnO_{3-\delta}$ films with an oxygen deficiency ($\delta \simeq 0.1$) and $La_{0.9}Ca_{0.1}MnO_3$ film with the stoichiometric oxygen content have been investigated in a wide temperature range.

It was shown that the COI state is observed for $La_{0.7}Ca_{0.3}MnO_{2.9}$ film with thickness $d \leq 30$ nm, which manifests mainly a cubic crystal structure with an anomalously small lattice parameter for this composition. In addition, the artificial compression of the crystal lattice due to the epitaxial growth of the film leads to a significant increase in the Curie temperature (down to the value which is typical for the stoichiometric composition) and to the recovery of magnetic ordering at high temperature. Increasing in the film thickness ($d \simeq 60$ nm) leads to a structural transition from the lattice-strained cubic to the relaxed rhombohedral phase, which is accompanied by a shift of the

Curie point to lower temperatures and a frustration of the COI state.

The magnetic and transport properties of the film with $d \simeq 60$ nm are similar to those exhibited by the optimally oxygen-doped $La_{0.9}Ca_{0.1}MnO_3$ film. This is confirmed by the roughly equal temperatures of the magnetic transition and the almost identical values of the activation energy. In contrast, the cubic modification of the $La_{0.7}Ca_{0.3}MnO_{2.9}$ film with $d \leq 30$ nm has a smaller value of the activation energy, which can be explained by the change in the Mn−O−Mn angle or the reduced distance between the Mn ions.

We conclude that the formation of the COI state in the oxygen-deficit $La_{0.9}Ca_{0.1}MnO_{3-\delta}$ films is governed by a compression of the crystal lattice rather than accumulation of the oxygen vacancies, the low doping of the substituted divalent ions, or electronic phase separation.

1. A. Biswas, M. Rajeswari, R.C. Srivastava, Y.H. Li, T. Venkatesan, R.L. Green, and A.J. Millis, *Phys. Rev.* **B61**, 9665 (2000).

2. A. Biswas, M. Rajeswari, R.C. Srivastava, T. Venkatesan, R.L. Green, Q. Lu, A.L. de Lozanne, and A.J. Millis, *cond-mat/0102321*.

3. M. Uehara, S. Mori, C.H. Chen, and S.-W. Cheong, *Nature* **399**, 560 (1999).

4. K.M. Satyalakshmi, S.S. Manoharan, M.S. Hegde, V. Prasad, and S.V. Subramanyam, *J. Appl. Phys.* **78**, 6861 (1995).

5. W. Zhang, W. Boyd, M. Elliot, and W. Herren-den-Harkerand, *Appl. Phys. Lett.* **69**, 3929 (1996).

6. J.-M. Liu and C.K. Ong, *Appl. Phys. Lett.* **73**, 1047 (1998).

7. R. Mahendiran, S.K. Tiwary, A.K. Raychaudhuri, and T.V. Ramakrishnan, *Phys. Rev.* **B53**, 3348 (1996).

8. J.-M. Liu and C. K. Ong, *J. Appl. Phys.* **84**, 5560 (1998).

9. J. Li, C.K. Ong, J.-M. Liu, Q. Huang, and S.J. Wang, *Appl. Phys. Lett.* **76**, 1051 (2000).

10. N. Abdelmoula, K. Guidara, A. Cheikh-Rouhou, E. Dhahri, and J.C. Joubert, *J. Solid State Chem.* **151**, 139 (2000).

11. J.R. Sun, C.F. Yeung, K. Zhao, L.Z. Zhuo, C.H. Leung, H.K. Wong, and B.G. Shen, *Appl. Phys. Lett.* **76**, 1164 (2000).

12. E. Dagotto, T. Hotta, and A. Moreo, *cond-mat/0012117*.

13. V.G. Prokhorov, G.G. Kaminsky, V.A. Komashko, J.S. Park, and Y.P. Lee, *J. Appl. Phys.* **90**, 1055 (2001).

14. K. Dörr, J.M. De Teresa, K.-H. Müller, D. Eckert, T. Walter, E. Vlakhov, and L. Schultz, *J. Phys.: Condens. Matter* **12**, 7099 (2000).

15. O.I. Lebedev, G. Van Tendeloo, S. Amelinkx, H.L. Ju, and K.M. Krishnan, *Philos. Mag.* **A80**, 673 (2000).

16. J. Aarts, S. Freibem, R. Hendrikx, and H.W. Zandbergen, *Appl. Phys. Lett.* **72**, 2975 (1998).

17. W.Z. Gong, B.R. Zhao, C. Cai, and Y. Lin, *Appl. Phys. Lett.* **79**, 827 (2001).

18. G. Biotteau, M. Hennion, F. Moussa, J. Rodriguez-Carvajal, L. Pinsard, and A. Revcolevschi, *Physica* **B259−261**, 826 (1999).

19. Y.P. Lee, V.G. Prokhorov, J.Y. Rhee, K.W. Kim, G.G. Kaminsky, and V.S. Flis, *J. Phys.: Condens. Matter* **12**, L133 (2000).

20. V.G. Prokhorov, G.G. Kaminsky, V.S. Flis, Y.P. Lee, K.W. Kim, and I.I. Kravchenko, *Physica* **B307**, 239 (2001).

21. Y.P. Lee, V.G. Prokhorov, K.W. Kim, and J.Y. Rhee, *J. Phys.: Condens. Matter* **13**, 9673 (2001).

22. G.H. Jonker and J.H. van Santen, *Physica* **19**, 120 (1953).

23. W. Prellier, M. Rajeswari, T. Venkatesan, and R.L. Greene, *Appl. Phys. Lett.* **75**, 1446 (1999).